American Mineralogist, Volume 92, pages 1190–1199, 2007

The high-pressure structural configurations of $Ca_{0.2}Sr_{0.8}Al_2Si_2O_8$ feldspar: The $I\bar{1}$-$I2/c$ and $I2/c$-$P2_1/c$ phase transitions

Piera Benna,[1,2,*] Fabrizio Nestola,[3] Tiziana Boffa Ballaran,[4] Tonči Balić-Žunić,[5] Lars Fahl Lundegaard,[6] and Emiliano Bruno[1]

[1]Dipartimento di Scienze Mineralogiche e Petrologiche, Via Valperga Caluso 35, I-10125 Torino, Italy
[2]Istituto di Geoscienze e Georisorse, CNR, Sezione di Torino, Italy
[3]Dipartimento di Mineralogia e Petrologia, Università di Padova, C.so Garibaldi 37, I-35137 Padova, Italy
[4]Bayerisches Geoinstitut, Universität Bayreuth, 95440 Bayreuth, Germany
[5]Geological Institute, University of Copenhagen, Øster Voldgade 10, DK-1350 Copenhagen K, Denmark
[6]Centre for Science at Extreme Conditions, University of Edinburgh, Mayfield Road, Edinburgh EH93JZ, U.K.

Abstract

Single-crystal in situ high-P X-ray diffraction was performed at P = 0.0001, 3.2, 4.4, 6.2, and 7.4 GPa on synthetic $Ca_{0.2}Sr_{0.8}Al_2Si_2O_8$ feldspar ($An_{20}SrF_{80}$). Data collections confirmed the displacive first-order triclinic $I\bar{1}$-monoclinic $I2/c$ phase transition at P ~4.3 GPa found in a previous high-P investigation and defined the first-order monoclinic-monoclinic transformation at P ~7.3 GPa as an $I2/c$-$P2_1/c$ symmetry change. The structural modifications induced by the increase of pressure inside the stability fields of $I\bar{1}$ and $I2/c$ configurations as well as the structural behavior of the two phase transitions were detailed. The $I\bar{1}$-$I2/c$ transition is similar to the displacive ferroelastic $I\bar{1}$-$I2/c$ phase transition observed for the same composition with increasing temperature and is related to the increase of the M-site coordination number, with the consequent regularization of Ca/Sr polyhedra and framework. Variations of the T-O-T bond angles are observed, whereas the O-T-O angles do not change significantly.

The $I2/c$-$P2_1/c$ transition involves a significant modification of the M-polyhedra. In the M(0)-polyhedron, the two O_C atoms, that were not coordinated in $I\bar{1}$ and $I2/c$ space groups, are now bonded more strongly than either O_B or O_D atoms [the M(0)-O_C(0i) and M(0)-O_C(zi) distances are 2.54 and 2.57 Å, respectively], whereas in the M(i)-polyhedron, it is the second OA(20) oxygen that becomes coordinated and, at the same time, one of the bonds to O_D atoms is broken. Moreover, a significant deformation of the framework is obtained due to the decrease of the symmetry from the loss of the two-fold axis and of half of the centers of symmetry. The transition induces, besides a significant distortion in the T-O-T bond angles, a deformation of the internal O-T-O angles within the tetrahedra. The T_2(00) tetrahedron, with the OA(20)-T_2(00)-O_C(0i) angle of 91° and the O_C(0i)-T_2(00)-O_D(0i) angle of 140°, is the most deformed.

Keywords: Crystal structure, high-pressure studies, phase transition, XRD data

Introduction

The feldspar structure has been well defined by crystallographic studies performed on natural and synthetic end-members and different solid solutions at both ambient conditions and at high temperatures and pressures (see the excellent reviews of Ribbe 1994 on crystal structure and of Angel 1994 and Ross 2000 on the high-pressure behaviors).

Structural investigations performed on alkali feldspars using high-pressure in situ single-crystal X-ray diffraction include those of Allan and Angel (1997) (microcline to P = 7 GPa), Downs et al. (1994), and Benusa et al. (2005) (compression of low albite to 4 GPa and 9.4 GPa, respectively). The structure of reedmergnerite has been refined by Downs et al. (1999) to 4.7 GPa. No phase transitions were observed in these feldspars with increasing pressure (the $C2/m$-$C\bar{1}$ transition observed in sanidine at P = 1.8 GPa by Hazen 1976 has not been confirmed). On the contrary, Angel et al. (1988) observed a reversible first-order $P\bar{1}$-$I\bar{1}$ phase transition between 2.6 and 3 GPa in anorthite. Angel (1988) determined the structural configurations of the $P\bar{1}$ and $I\bar{1}$ phases by means of in situ structural investigations at high-pressure.

Recently, Nestola et al. (2004) observed pressure induced phase transitions in a feldspar of composition $Ca_{0.2}Sr_{0.8}Al_2Si_2O_8$, which lies on the solid solution between triclinic $P\bar{1}$ anorthite (An, $CaAl_2Si_2O_8$) and monoclinic $I2/c$ Sr-feldspar (SrF, $SrAl_2Si_2O_8$). Along this join at ambient conditions the symmetry changes from $I\bar{1}$ to $I2/c$ at a composition of ~$An_{10}SrF_{90}$. Moreover, feldspars with compositions between $An_{40}SrF_{60}$ and $An_{10}SrF_{90}$ undergo the analogous $I\bar{1}$-$I2/c$ transition with increasing temperature. The $I\bar{1}$-$I2/c$ phase transition (Bruno and Gazzoni 1968; Nager 1969; Nager et al. 1969; Tribaudino et al. 1993)

* E-mail: piera.benna@unito.it

was defined as a zone-center displacive ferroelastic transition (McGuinn and Redfern 1994; Dove and Redfern 1997). Benna and Bruno (2003) studied the structural modifications occurring in the $I\bar{1}$-$I2/c$ transition, induced by the increase of temperature in the feldspar of composition $An_{20}SrF_{80}$, by in situ single-crystal X-ray diffraction (Ttr ~520 °C).

Nestola et al. (2004), using crystals of similar composition, measured unit-cell parameters as a function of pressure (P range = 0.0001–7.7 GPa) by in situ single-crystal X-ray diffraction. Two reversible phase transitions were observed. A first-order triclinic $I\bar{1}$ to monoclinic $I2/c$ phase transition was observed at P ~4.3 GPa, similar to the $I\bar{1}$-$I2/c$ transition of second-order observed for the same sample with increasing temperature (Benna and Bruno 2003). At P ~7.3 GPa a further strongly first-order transition, from monoclinic $I2/c$ phase to monoclinic-II phase, was observed. The volume bulk modulus is K_0 = 88.7(5) GPa for the $I\bar{1}$ triclinic phase and K_0 = 89.4(9) GPa for the $I2/c$ monoclinic phase. These values are very close to the value of 83 GPa of well-ordered anorthite (Hackwell and Angel 1992; Angel 1994; Ross 2000) and significantly higher than that of range of moduli of albite, sanidine and microcline between 54 and 70 GPa (Angel et al. 1988; Hackwell 1993; Downs et al. 1994; Allan and Angel 1997; Benusa et al. 2005).

Even if feldspars are stable in an extremely limited pressure range under geological conditions, investigations on structural modifications and phase transitions induced by pressure provide much needed data on thermodynamic properties (Angel 1994).

In this work, in situ high-P single-crystal X-ray data have been collected on a crystal of composition $An_{20}SrF_{80}$ to define the structural changes that take place with increasing pressure and, in particular, the modifications occurring when monoclinic symmetry is achieved after the first and the second transition.

Experimental methods

The crystal of composition $Ca_{0.2}Sr_{0.8}Al_2Si_2O_8$ studied in this work has an Al-Si order described by the order parameter Q_{od} = 0.88, and is from the same run product used for the high-T single-crystal investigation of Benna and Bruno (2003) and high-P investigation of Nestola et al. (2004). The unit-cell parameters measured at room conditions for this crystal using a Huber four-circle diffractometer and the eight-position centering method of King and Finger (1979) were found to be within one standard deviation with respect to those reported by Nestola et al. (2004). Subsequently, the crystal (dimensions 250 × 150 × 60 µm) was loaded in a BGI design diamond-anvil cell (Allan et al. 1996), using a steel gasket (T301) and a 16:3:1 mixture of methanol:ethanol:water as pressure transmitting medium. The gasket was previously preindented to 100 µm thickness and the gasket hole was 350 µm in diameter. A ruby chip was used as an internal diffraction pressure standard.

Five complete intensity data collections were performed at P = 0.0001, 3.2, 4.4, 6.2, and 7.4 GPa using a Bruker-AXS four-circle diffractometer equipped with a Smart1000 CCD area detector (6.25 × 6.25 cm active area with a resolution of 81.92 pixels cm^{-1}) and a flat graphite monochromator, using Mo$K\alpha$ radiation. The sample-to-detector distance was 5.5 cm. A total of 1800 exposures (frame width = 0.2°, time = 60 s) were collected at every pressure in 16 separate ω-scans covering practically all of the available reciprocal space. Each scan covered a span of 20° in ω with detector (2θ circle) positioned so as to be parallel to the planes of the gasket and culet faces in the middle of the scan range. This orientation of the detector relative to DAC avoids completely the blind regions (secondary X-rays shaded by the DAC body) at the applied sample-detector distance. Eight of the scans were performed with ϕ setting adjusted so that the primary beam was entering one side of the DAC; the other eight with ϕ setting 180° apart with the primary beam entering the other side of DAC first. In this way optimal conditions are ensured for the refinement of the crystal displacement from the goniometer center. In each group of runs, four were performed with χ set to 0° which makes ϕ and ω axes coincident, summing to a total sweep angle for the primary beam of 80° from both sides of the DAC, covering close to a full opening angle of the beryllium window. The remaining scans were performed with χ set to various angles ensuring the best coverage of the rest of the unshaded reciprocal space. The SMART software was used for the lattice determination and data collection. The data were integrated with SAINT+ and corrected for the absorption using SADABS softwares (Bruker 2000) getting a significant improvement in R_{int}. SADABS correction was applied for the complex absorption effects, where an empirical function based on measurements of symmetry equivalents (over 800 reflections with I > 3σ) and applying a function modeled upon spherical harmonics (maximum odd and even orders of 3 and 6, respectively) was used. SADABS also removes the "outlier" reflections with $|I - \langle I\rangle|/[\sigma^2 + (0.04 \langle I\rangle)^2] > 4$.

The measurements at room pressure and at 3.2 GPa were performed to define the structural modifications before the $I\bar{1}$-$I2/c$ phase transition, within the $I\bar{1}$ space group, whereas the data collected at 4.4 and 6.2 GPa are relative to the $I2/c$ space group. These data collections show only a and b-type reflections (a-type reflections: $h + k$ = even, l = even; b-type reflections: $h + k$ = odd, l = odd) confirming the $I\bar{1}$ and the $I2/c$ space groups as in Nestola et al. (2004). At 7.4 GPa, where Nestola et al. (2004) observed the monoclinic-II phase, the data collection also shows the presence of c- and d-type reflections (c-type reflections: $h + k$ = even, l = odd; d-type reflections: $h + k$ = odd, l = even) indicating a primitive lattice. In contrast to $P\bar{1}$ anorthite (Kempster et al. 1962), the scheme of intensity of the different reflections in the present work is: $a > d > b \geq c$. Reflections $h0l$ and $00l$ with l = even only were observed. Unfortunately, because of the crystal shape and its orientation in the DAC, it has not been possible to measure diffractions of the $0k0$ type to verify the presence of a screw axis along the **b** direction. Several primitive space groups were therefore tested. The best results were obtained using the $P2_1/c$ space group.

Weighted structural refinements were done using the SHELX-97 package (Sheldrick 1997). The refinements were performed in $I\bar{1}$ (P = 1 atm and 3.2 GPa), $I2/c$ (P = 4.4 and 6.2 GPa) and $P2_1/c$ (P = 7.4 GPa) space groups, starting from the atomic coordinates of Benna and Bruno (2003) at room temperature for the data collected at P = 1 atm and 3.2 GPa and from the atomic coordinates at T = 600 °C (HT monoclinic symmetry) for the data collected at P = 4.4 and 6.2 GPa. At 7.4 GPa, all the atoms of $I2/c$ symmetry were split in two non-equivalent sites taking into account the change of origin by ¼, ¼, ¼ in the $P2_1/c$ space group. For all the refinements, anisotropic displacement parameters were introduced only for extra-framework Ca/Sr cations. The relative occupancies of Ca and Sr (0.2 and 0.8 apfu, respectively) did not change significantly in the refinements up to the maximum pressure reached and have been fixed to the nominal values in the final cycles.

Unit-cell parameters and refinement details are reported in Table 1. The R-factors for both $I2/c$ refinements are significantly poorer than those for the refinements of the $I\bar{1}$ and $P2_1/c$ structures. Since in the $I2/c$ refinements the shape of reflections does not suggest any splitting due to lower symmetry of the lattice, we conclude that $I2/c$ is the correct space group and the somewhat poorer results might be attributed to the very low intensity of b-type reflections (Table 1).

Fractional atomic coordinates and displacement parameters are shown in Table 2. The displacement ellipsoid for the M-site atom in $I2/c$ model is disc-shaped, and flattened along the **b**-axis. An attempt to refine a "split" position for this atom did not improve the refinement and the R-factors did not change. M-O interatomic distances and O-T-O bond angles are listed in Tables 3 and 4 respectively, whereas T-O interatomic distances, T-O-T angles and observed and calculated structure factors are reported in Tables 5[1], 6[1], and 7[1].

Results and discussion

HP evolution of the $I\bar{1}$ configuration and $I\bar{1}$-$I2/c$ transition

The comparison between the structural results obtained at P = 1 atm and at 3.2 GPa shows a significant modification of M-O bond lengths and a variation of T-O-T bond angles, while

[1] Deposit item AM-07-024, Tables 5, 6, and 7 (various measurements). Deposit items are available two ways: For a paper copy contact the Business Office of the Mineralogical Society of America (see inside front cover of recent issue) for price information. For an electronic copy visit the MSA web site at http://www.minsocam.org, go to the American Mineralogist Contents, find the table of contents for the specific volume/issue wanted, and then click on the deposit link there.

T-O distances and O-T-O angles do not change significantly. Analogous behavior was observed in anorthite between 1 atm and 2.5 GPa by Angel (1988), who interpreted the reduction of Ca-O bond distances arising from small flexures of the T-O-T angles between essentially rigid tetrahedra. In $An_{20}SrF_{80}$ feldspar, the increase of pressure to 3.2 GPa causes a reduction of the average <M-O> bond distances from 2.65 to 2.59 Å for the M(0)-polyhedron and from 2.64 to 2.62 Å for the M(z)-polyhedron, considering a sixfold coordination (Table 3). At 3.2 GPa these polyhedra show a configuration not much different from that at room pressure.

In Figure 1 the main structural features along **a*** direction (Bruno and Facchinelli 1974) are reported at different pressures. The figure shows the $O_A(2)$-M-M-$O_A(2)$ "strut" that Megaw (1970) suggested held the crankshaft chains open. The fact that this "strut" lies parallel to the most compressible direction (the (100) plane normal) of feldspars was used as an argument by Angel et al. (1988), who claimed that it only plays a passive role in the feldspar structure, a conclusion that is borne out by the results reported here as well as by Benusa et al. (2005). In the triclinic structure (Fig.1a) the $O_A(2)$-$O_A(2)$ distances across the M-polyhedra decrease from 8.88 Å ($\overline{AB}$ distance in M(z)-polyhe-

Table 1. Single-crystal data at different pressures (e.s.d. values in brackets)

P (GPa)	0.0001	3.2	4.4	6.2	7.4
Space group	$I\bar{1}$	$I\bar{1}$	*I*2/*c*	*I*2/*c*	$P2_1/c$
a (Å)	8.370(1)	8.256(1)	8.209(1)	8.128(1)	8.116(0)
b (Å)	12.967(1)	12.842(1)	12.780(2)	12.671(2)	12.410(1)
c (Å)	14.262(1)	14.088(1)	14.009(1)	13.866(1)	13.728(1)
α (°)	90.58(1)	90.51(1)	90	90	90
β (°)	115.55(1)	115.38(1)	115.27(1)	114.98(1)	114.19(0)
γ (°)	90.44(1)	90.88(1)	90	90	90
V (Å^3)	1396.5	1349.3	1328.9	1294.4	1261.3
μ (mm^{-1})	6.96	7.21	7.32	7.51	7.71
Unique reflections	775	1143	518	549	1009
Refl. observed $F_o \geq 2\sigma(F_o)$	522	717	309	293	759
Refl. *a*-type $F_o \geq 2\sigma(F_o)$	345	509	226	213	251
Refl. *b*-type $F_o \geq 2\sigma(F_o)$	177	208	83	85	148
Refl. *c*-type $F_o \geq 2\sigma(F_o)$	–	–	–	–	116
Refl. *d*-type $F_o \geq 2\sigma(F_o)$	–	–	–	–	245
No. refl. *b*/No. refl. *a*	0.513	0.409	0.367	0.399	0.586
$\Sigma F^2_{o(b)}/\Sigma F^2_{o(a)}$	0.025	0.023	0.012	0.018	0.032
R	0.073	0.095	0.140	0.192	0.089
$R\ F_o \geq 2\sigma(F_o)$	0.045	0.052	0.093	0.115	0.059
$R\ F_o \geq 4\sigma(F_o)$	0.039	0.043	0.083	0.107	0.048
wR^2	0.098	0.108	0.244	0.342	0.131
Weights	0.06	0.06	0.10	0.20	0.07
Goodness of fit	0.87	0.89	1.44	1.05	1.02

Note: $w = 1/[\sigma^2(F_o^2) + (a \cdot P)^2]$, where $P = (F_o^2 + 2F_c^2)/3$.

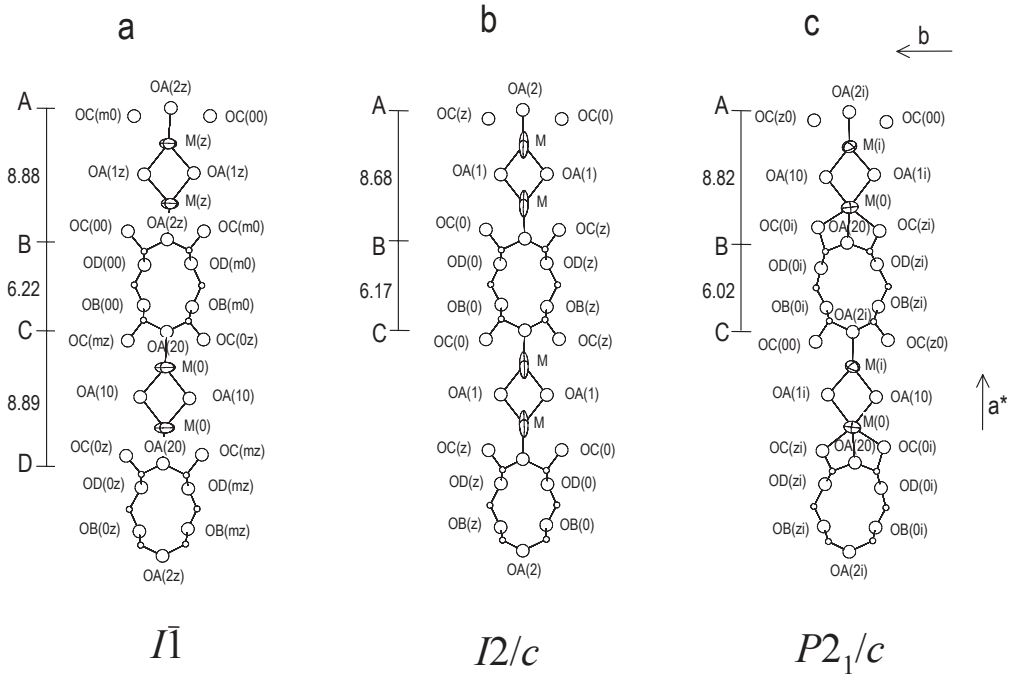

Figure 1. A slice of the $An_{20}SrF_{80}$ feldspar structure viewed approximately along the **c** axis (thickness ~2.5 Å) showing the $O_A(2)$-M-M-$O_A(2)$ "strut," Megaw (1970). $\overline{AB}$ and $\overline{CD}$ = $O_A(2)$-$O_A(2)$ distances (Å) across M-polyhedra. $\overline{BC}$ = $O_A(2)$-$O_A(2)$ distances (Å) across the tetrahedral cage. Tetrahedral T atoms are not labeled. (**a**) *P* = 1 atm; (**b**) *P* = 4.4 GPa; (**c**) *P* = 7.4 GPa.

TABLE 2. Atomic fractional coordinates (×10⁴) and isotropic displacement parameters (Å² × 10³)

Site	x	y	z	U_{eq}/U^*	Site	x	y	z	U_{eq}/U^*
		P = 0.0001 GPa	$I\bar{1}$ space group				P = 3.2 GPa	$I\bar{1}$ space group	
Ca/Sr(0)	2691(1)	1(3)	669(1)	15(3)	Ca/Sr(0)	2675(1)	33(2)	674(1)	19(2)
Ca/Sr(z)	2676(1)	64(3)	5636(1)	9(3)	Ca/Sr(z)	2662(1)	59(2)	5645(1)	13(2)
T_1(00)	70(4)	1710(9)	1070(2)	8(1)	T_1(00)	23(4)	1691(8)	1061(2)	10(1)
T_1(0z)	23(4)	1759(9)	6156(2)	9(1)	T_1(0z)	9992(4)	1725(8)	6154(2)	9(1)
T_1(m0)	30(4)	8182(11)	1179(2)	9(1)	T_1(m0)	9985(4)	8182(8)	1176(2)	11(1)
T_1(mz)	62(4)	8246(11)	6088(2)	11(1)	T_1(mz)	16(4)	8193(8)	6084(2)	9(1)
T_2(00)	6920(4)	1197(8)	1675(2)	9(1)	T_2(00)	6881(4)	1198(8)	1674(2)	10(1)
T_2(0z)	6827(4)	1124(8)	6687(2)	12(1)	T_2(0z)	6790(4)	1105(7)	6678(2)	11(1)
T_2(m0)	6839(4)	8847(8)	1745(2)	11(1)	T_2(m0)	6793(4)	8841(7)	1751(2)	10(1)
T_2(mz)	6933(4)	8792(8)	6722(2)	10(1)	T_2(mz)	6883(4)	8765(7)	6724(2)	10(1)
O_A(10)	69(8)	1305(14)	9998(4)	15(2)	O_A(10)	31(8)	1260(13)	9972(4)	13(2)
O_A(1z)	9948(8)	1283(14)	4969(4)	15(2)	O_A(1z)	9964(8)	1336(13)	4981(4)	14(2)
O_A(20)	5885(9)	9997(8)	1420(5)	17(2)	O_A(20)	5829(10)	9929(15)	1433(5)	19(2)
O_A(2z)	5875(9)	2(8)	6414(5)	12(2)	O_A(2z)	5829(10)	9972(15)	6450(5)	18(2)
O_B(00)	8260(8)	1224(16)	1011(5)	14(2)	O_B(00)	8209(9)	1125(14)	991(5)	19(2)
O_B(0z)	8078(9)	1189(17)	6073(5)	15(2)	O_B(0z)	7996(9)	1188(14)	6028(5)	17(2)
O_B(m0)	8071(9)	8698(17)	1151(5)	19(2)	O_B(m0)	8018(9)	8642(15)	1127(5)	17(2)
O_B(mz)	8263(9)	8658(17)	6077(4)	15(2)	O_B(mz)	8210(9)	8674(14)	6068(5)	17(2)
O_C(00)	162(10)	2951(11)	1241(6)	20(3)	O_C(00)	43(9)	2967(17)	1214(5)	12(2)
O_C(0z)	188(10)	3081(11)	6372(6)	20(2)	O_C(0z)	116(9)	3035(16)	6397(6)	17(2)
O_C(m0)	137(10)	6886(14)	1248(5)	21(3)	O_C(m0)	72(10)	6864(17)	1228(5)	19(2)
O_C(mz)	94(9)	6979(13)	6119(5)	15(3)	O_C(mz)	9987(9)	6913(17)	6116(5)	18(2)
O_D(00)	1856(9)	1182(18)	1939(5)	16(2)	O_D(00)	1860(9)	1209(15)	1925(5)	15(2)
O_D(0z)	1973(9)	1093(18)	7004(5)	20(2)	O_D(0z)	1966(9)	1167(15)	7001(5)	18(2)
O_D(m0)	1976(8)	8779(18)	2070(4)	12(2)	O_D(m0)	1977(9)	8768(15)	2084(5)	17(2)
O_D(mz)	1871(9)	8716(19)	6986(5)	18(2)	O_D(mz)	1877(9)	8713(15)	6994(5)	17(2)
		P = 4.4 GPa	$I2/c$ space group				P = 6.2 GPa	$I2/c$ space group	
Ca/Sr	2672(2)	−5(4)	671(1)	29(4)	Ca/Sr	2654(3)	9(4)	685(2)	43(4)
T_1(0)	9993(6)	1743(15)	1071(4)	37(2)	T_1(0)	9955(7)	1773(12)	1070(4)	44(2)
T_1(z)	9964(6)	1785(14)	6169(4)	33(2)	T_1(z)	9933(7)	1755(12)	6176(5)	43(2)
T_2(0)	6870(6)	1198(11)	1703(4)	35(2)	T_2(0)	6844(8)	1243(12)	1707(5)	41(2)
T_2(z)	6794(6)	1125(12)	6721(4)	36(2)	T_2(z)	6748(8)	1131(12)	6720(5)	44(2)
O_A(1)	19(10)	1267(27)	9978(7)	38(4)	O_A(1)	27(10)	1293(27)	9981(7)	34(4)
O_A(2)	5857(18)	9950(16)	1473(10)	46(4)	O_A(2)	5812(22)	33(14)	1482(15)	55(5)
O_B(0)	8185(14)	1205(26)	1025(9)	42(3)	O_B(0)	8186(17)	1180(28)	1045(12)	60(5)
O_B(z)	7976(15)	1255(27)	6075(9)	44(4)	O_B(z)	7940(17)	1171(25)	6048(11)	54(4)
O_C(0)	12(14)	3004(18)	1177(9)	47(5)	O_C(0)	9884(17)	3034(18)	1141(11)	54(6)
O_C(z)	51(15)	3135(18)	6311(10)	56(5)	O_C(z)	9955(17)	3115(16)	6267(11)	55(5)
O_D(0)	1864(15)	1248(28)	1975(9)	47(4)	O_D(0)	1832(17)	1249(28)	1943(10)	54(4)
O_D(z)	1932(15)	1207(27)	7052(9)	48(4)	O_D(z)	1915(16)	1171(25)	7020(10)	56(5)
		P = 7.4 GPa	$P2_1/c$ space group†						
Ca/Sr(0)	2893(1)	71(3)	642(1)	15(2)					
Ca/Sr(i)	7620(1)	4917(3)	5729(1)	15(2)					
T_1(00)	9975(4)	1767(8)	1135(2)	12(1)					
T_1(0i)	4781(3)	6895(8)	5947(2)	12(1)					
T_1(z0)	20(4)	1635(8)	6232(3)	14(1)					
T_1(zi)	4899(4)	7018(8)	1102(2)	10(1)					
T_2(00)	6910(4)	1390(8)	1791(2)	11(1)					
T_2(0i)	1774(4)	6179(8)	6664(2)	11(1)					
T_2(z0)	6893(4)	1021(7)	6851(2)	12(1)					
T_2(zi)	1707(4)	6226(7)	1735(2)	12(1)					
O_A(10)	152(8)	1356(17)	32(5)	13(2)					
O_A(1i)	5068(8)	6257(18)	5006(5)	19(2)					
O_A(20)	6121(9)	211(16)	2015(6)	25(2)					
O_A(2i)	775(9)	4906(17)	6225(5)	23(2)					
O_B(00)	8138(9)	1229(17)	1016(5)	19(2)					
O_B(0i)	2978(10)	6332(17)	5910(6)	27(2)					
O_B(z0)	8071(9)	1006(16)	6171(6)	23(2)					
O_B(zi)	3075(10)	6482(17)	1200(6)	27(2)					
O_C(00)	9873(9)	3078(17)	1285(5)	21(2)					
O_C(0i)	4717(9)	8210(19)	5894(6)	29(3)					
O_C(z0)	21(9)	2998(17)	6446(6)	25(2)					
O_C(zi)	5045(9)	8451(18)	1174(5)	18(2)					
O_D(00)	1833(9)	1264(17)	2024(6)	25(2)					
O_D(0i)	6577(10)	6628(19)	6966(6)	39(3)					
O_D(z0)	2147(8)	1113(15)	7010(5)	18(2)					
O_D(zi)	6923(8)	6411(16)	1973(5)	18(2)					

* All atoms except for Ca/Sr were refined with isotropic displacement parameters. U_{eq} defined as one third of the trace of the orthogonalized U_{ij} tensor. The isotropic displacement exponent takes the form: $-8\pi^2 U(\sin\theta/\lambda)^2$. Occupancies of Ca and Sr on both sites are 0.2 and 0.8, respectively.

† The coordinates of the $P2_1/c$ model have been reported without the ¼, ¼, ¼ origin shift to compare our data with those of other feldspar structures. The symmetry operators for this non-standard setting must be changed accordingly.

TABLE 3. M-O interatomic distances (Å)

P (GPa)	0.0001	3.2		4.4	6.2		7.4
Space group	*I*$\bar{1}$	*I*$\bar{1}$		*I*2/*c*	*I*2/*c*		*P*2$_1$/*c*
M(0)-OA(10)	2.621(14)	2.551(11)				M(0)-OA(10)	2.583(14)
M(0)-OA(10)	2.668(12)	2.588(12)				M(0)-OA(1i)	2.744(14)
M(0)-OA(20)	2.414(7)	2.359(8)				M(0)-OA(20)	2.529(7)
M(0)-OB(00)	2.675(13)	2.585(12)				M(0)-OA(2i)	3.163(8)
M(0)-OB(m0)	2.944(14)	2.919(12)				M(0)-OB(0i)	2.616(15)
M(0)-OC(0z)	3.146(12)	3.183(17)				M(0)-OB(zi)	2.906(14)
M(0)-OC(mz)	3.168(15)	2.945(19)				M(0)-OC(0i)	2.538(21)
M(0)-OD(00)	2.677(15)	2.616(12)	M-OA(1)	2.553(22)	2.529(23)	M(0)-OC(zi)	2.566(19)
M(0)-OD(m0)	2.819(13)	2.817(11)	M-OA(1)	2.568(22)	2.573(22)	M(0)-OD(00)	2.804(13)
<[6]M(0)-O>	2.646	2.586	M-OA(2)	2.365(14)	2.327(17)	M(0)-OD(z0)	2.643(12)
<[7]M(0)-O>	2.688	2.633	M-OB(0)	2.658(21)	2.665(23)	<[7]M(0)-O>	2.603
			M-OB(z)	2.783 (22)	2.682(22)	<[8]M(0)-O>	2.628
			M-OC(0)	3.093(22)	2.977(22)	<[9]M(0)-O>	2.659
			M-OC(z)	2.962(21)	2.938(19)		
M(z)-OA(1z)	2.613(13)	2.627(13)	M-OD(0)	2.715(22)	2.636(24)	M(i)-OA(10)	2.593(14)
M(z)-OA(1z)	2.626(13)	2.624(11)	M-OD(z)	2.734(21)	2.639(22)	M(i)-OA(1i)	2.521(15)
M(z)-OA(2z)	2.419(7)	2.368(8)	<[6]M-O>	2.599	2.562	M(i)-OA(20)	2.860(7)
M(z)-OB(0z)	2.749(14)	2.687(12)	<[7]M-O>	2.625	2.579	M(i)-OA(2i)	2.365(7)
M(z)-OB(mz)	2.789(15)	2.758(11)				M(i)-OB(00)	2.633(13)
M(z)-OC(00)	3.343(13)	3.251(18)				M(i)-OB(z0)	2.782(12)
M(z)-OC(m0)	2.986(14)	2.903(18)				M(i)-OC(00)	2.995(19)
M(z)-OD(0z)	2.623(13)	2.631(11)				M(i)-OC(z0)	2.978(18)
M(z)-OD(mz)	2.896(15)	2.846(12)				M(i)-OD(0i)	3.048(17)
<[6]M(z)-O>	2.636	2.616				M(i)-OD(zi)	2.597(14)
<[7]M(z)-O>	2.674	2.649				<[7]M(i)-O>	2.622
						<[8]M(i)-O>	2.666
						<[9]M(i)-O>	2.703

TABLE 4. O-T-O angles (°)

	OA-OB	OA-OC	OA-OD	OB-OC	OB-OD	OC-OD
			P = 0.0001 GPa			
T_1(00)	102.4(6)	115.9(8)	102.0(7)	111.8(8)	114.0(10)	110.3(9)
T_1(0z)	98.5(6)	118.1(7)	97.1(6)	115.1(8)	113.1(9)	113.0(8)
T_1(m0)	99.5(7)	114.7(7)	99.9(7)	114.4(9)	114.8(10)	112.1(9)
T_1(mz)	103.3(8)	114.2(8)	102.9(8)	110.2(9)	116.2(10)	109.7(10)
T_2(00)	106.5(8)	101.2(6)	106.0(9)	112.7(7)	112.8(4)	116.2(8)
T_2(0z)	106.4(9)	101.8(6)	109.1(10)	114.5(8)	110.3(4)	114.1(9)
T_2(m0)	107.5(9)	102.6(5)	105.6(10)	114.4(8)	110.8(4)	114.8(8)
T_2(mz)	108.9(8)	101.9(5)	105.2(9)	111.6(7)	112.4(4)	115.9(8)
			P = 3.2 GPa			
T_1(00)	100.1(6)	116.6(7)	101.1(6)	113.4(7)	114.5(8)	110.4(8)
T_1(0z)	100.1(5)	116.5(7)	99.3(5)	112.0(7)	119.0(8)	109.4(7)
T_1(m0)	100.3(5)	115.9(6)	97.8(6)	112.6(7)	117.5(8)	111.7(7)
T_1(mz)	102.1(6)	114.2(7)	101.3(6)	111.9(7)	114.0(8)	112.5(7)
T_2(00)	102.2(8)	98.0(7)	105.3(8)	116.6(5)	112.6(4)	118.6(7)
T_2(0z)	108.2(8)	101.6(7)	108.6(9)	112.8(7)	110.6(4)	114.4(8)
T_2(m0)	110.2(7)	102.1(7)	109.7(9)	112.6(8)	109.6(4)	112.4(8)
T_2(mz)	108.5(7)	99.3(6)	104.4(8)	113.0(7)	111.9(4)	118.1(7)
			P = 4.4 GPa			
T_1(0)	100.5(12)	116.6(14)	101.2(11)	113.7(13)	114.1(15)	110.1(14)
T_1(z)	99.2(11)	117.9(13)	97.2(11)	113.0(13)	117.0(14)	111.3(13)
T_2(0)	105.2(13)	101.3(9)	104.8(15)	114.4(10)	111.6(7)	117.7(12)
T_2(z)	109.4(14)	99.3(10)	109.7(16)	113.7(12)	109.2(7)	115.0(13)
			P = 6.2 GPa			
T_1(0)	100.6(12)	116.1(14)	98.3(11)	114.3(13)	111.8(14)	113.9(13)
T_1(z)	98.3(10)	113.8(14)	96.2(10)	114.6(12)	117.3(13)	113.8(12)
T_2(0)	103.8(14)	96.1(9)	103.5(15)	117.6(11)	109.8(8)	121.9(12)
T_2(z)	104.9(15)	100.8(9)	106.8(15)	114.8(13)	109.3(8)	118.7(13)
			P = 7.4 GPa			
T_1(00)	102.0(7)	116.4(9)	99.6(6)	109.7(8)	117.5(9)	111.3(8)
T_1(0i)	101.0(9)	117.9(8)	102.8(7)	115.0(9)	115.7(8)	104.4(9)
T_1(z0)	99.2(7)	115.6(9)	97.6(6)	112.8(8)	121.2(9)	109.3(7)
T_1(zi)	100.7(8)	119.7(8)	94.6(7)	115.6(8)	112.6(8)	111.6(7)
T_2(00)	111.7(10)	91.2(8)	98.3(8)	105.7(4)	106.2(4)	140.4(10)
T_2(0i)	100.9(8)	98.6(8)	115.6(10)	115.6(8)	109.9(4)	115.0(7)
T_2(z0)	114.3(10)	98.1(8)	104.1(8)	108.6(5)	110.2(5)	121.2(9)
T_2(zi)	105.3(8)	102.6(8)	110.8(10)	117.1(9)	107.9(4)	112.7(7)

dron) and 8.89 Å [$\overline{CD}$ in M(0)-polyhedron] at *P* = 1 atm to ~8.70 Å at *P* = 3.2 GPa. The compression of the M-M distance, together with the significant decrease of the M-O_A(2) distances (Table 3), accounts for the overall decrease of the "strut" along **a***.

The orientation of the principal axes of the strain ellipsoid (Fig. 2), calculated from the cell parameters in the *P* range 1 atm–4.3 GPa (Nestola et al. 2004), is very similar to that determined by Angel et al. (1988) for anorthite between 1 atm and 5 GPa, and is quite different from that of alkali feldspars. In fact, the plane containing the axes of maximum (ε_1) and minimum (ε_3) compression is about 15° from the (001) plane. As observed by Angel (1994), the orientation of the direction of maximum compression close to (001) plane is consistent with the increase of the γ angle with increasing pressure. While in anorthite the unit strain ellipsoid is strongly anisotropic (ε_1 = 71, ε_2 = 24, and ε_3 = 7

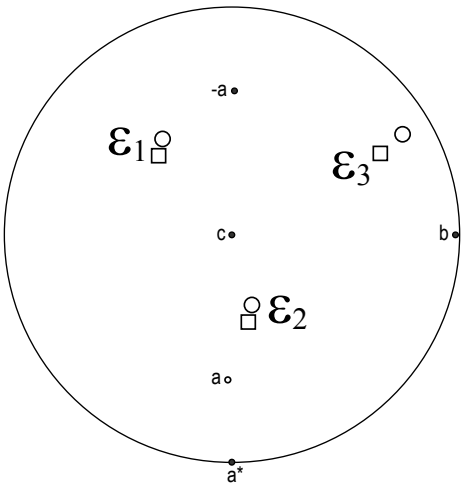

FIGURE 2. Stereographic projection showing the orientation of the principal axes, ε_1, ε_2, and ε_3 of the strain ellipsoid describing the behavior upon compression. Circles: $An_{20}SrF_{80}$ feldspar, pressure range = 1 atm – 4.3 GPa (Nestola et al. 2004). Squares: anorthite, pressure range = 1 atm – 5 GPa (Angel et al. 1988). The **a**, **b**, **c** direct lattice vectors and the **a*** reciprocal vector are relative to $An_{20}SrF_{80}$ feldspar. All axes are plotted in the upper hemisphere, except for +**a**.

$\times 10^4$ GPa^{-1}), in $An_{20}SrF_{80}$ feldspar the anisotropy is drastically reduced ($\varepsilon_1 = 49$, $\varepsilon_2 = 33$, and $\varepsilon_3 = 26 \times 10^4$ GPa^{-1}).

At the $I\bar{1}$-$I2/c$ phase transition, the 8 independent T-sites in the triclinic structure are reduced to 4 T-sites in the monoclinic one (Table 2). This is summarized in Figure 3, where the pairs of pseudo-symmetrical T-sites in the $I\bar{1}$ configuration converge to single T-sites in the $I2/c$ configuration. The transition involves pairs of chemically homogenous tetrahedra that do not significantly vary their average sizes with increasing pressure (Table 5[1]). Consequently, the alternation of Si- and Al-rich tetrahedra observed in the triclinic configuration is maintained in the monoclinic configuration.

At the transition the O-T-O angles show no significant changes (Table 4), while greater modifications are observed in the T-O-T bond angles. While the average <T-O_D-T> angles increase, the <T-O_A-T>, <T-O_B-T>, and <T-O_C-T> angles decrease or remain constant (Fig. 4). As expected in non-collapsible framework such as feldspar (Baur et al. 1996; Angel et al. 2005), although the decrease of the average <T-O-T> angle with pressure is relatively small, individual T-O-T bond angles show a large variations, with some increasing and some decreasing, as typical for other feldspars studied at high pressures (Ross 2000). The more relevant changes are the decrease in individual T-O-T angles relative to O_A(1z), O_B(m0), and O_B(mz) oxygen atoms and an increase in those relative to O_C(mz) and O_D(0z) oxygen atoms (Table 6[1]).

For the non-tetrahedral Ca/Sr cations, the two independent M(0)- and M(z)-polyhedra in the triclinic structure (Fig. 5a) become equivalent and a single M-polyhedron is observed in the $I2/c$ monoclinic structure (Fig. 5b). At the $I\bar{1}$-$I2/c$ transition,

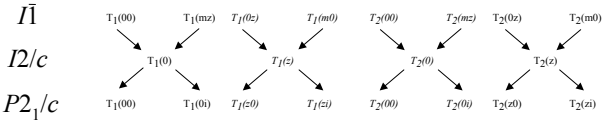

FIGURE 3. Tetrahedral T-sites nomenclature for the $I\bar{1}$, $I2/c$, and $P2_1/c$ configurations. The Al-rich T-sites are in italic.

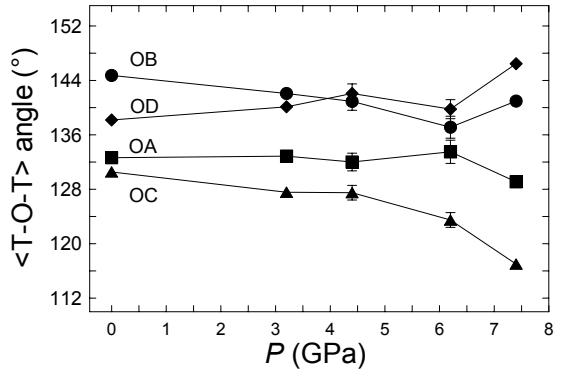

FIGURE 4. The variation of the average <T-O-T> bond angles with pressure. Squares: <T-O_A-T>, circles: <T-O_B-T>, triangles: <T-O_C-T>, diamonds: <T-O_D-T>. The lines are drawn as guides to the eye. Symbol size exceeds the estimated standard deviations (e.s.d. values), except at $P = 4.4$ and 6.2 GPa.

all pseudo-related oxygen pairs become equivalent and there is the passage from 16 to 8 independent oxygen atoms. In Figure 6 the modifications induced in the M-O distances by the transition for the pseudo-related O_B, O_C, and O_D oxygen pairs are shown. The lines in the figure are just guidelines to point out the discontinuity induced by the first-order $I\bar{1}$-$I2/c$ transition. The transition from triclinic to monoclinic symmetry gives rise to a more regular polyhedron around the Ca/Sr cations (Table 3, Fig. 5). The O_B(z) and O_D(0) oxygen atoms (Fig. 5b), corresponding in the triclinic structure to O_B(m0) in M(0) and O_D(mz) in M(z)-polyhedra (Fig. 5a), are involved in the increase of the coordination number and show the more significant variations among the M-O distances (Fig. 6).

The $I2/c$ configuration is analogous to that obtained with increasing temperature in a feldspar with the same composition (Benna and Bruno 2003). In the continuous high-T transition the α and γ unit-cell angles and the M-O distances show a continuous trend toward the monoclinic symmetry with increasing temperature. In the discontinuous high-P transition the γ angle (90.55° at P = 1 atm) achieves the values of 91.04° before jumping to 90°, as shown in Figure 1 of Nestola et al. (2004). Moreover, the differences between the M-O distances relative to the pseudo-related oxygen pairs are almost constant up to the transition (Fig. 6).

Both high-temperature and high-pressure $I2/c$ monoclinic structures are characterized by an increase of the coordination number of the Ca/Sr cations, which can be ascribed to an increase of the r_C/r_O ratio, where r_C is the ionic radius of the non-tetrahedral cations and r_O is the ionic radius of oxygen. At HP the higher compressibility of the oxygen atoms with respect to the non-tetrahedral cations gives rise to the increase of the r_C/r_O ratio and causes the triclinic-monoclinic transition. This is in agreement with the observation by Prewitt and Downs (1998) "increasing pressure increases coordination number" and, more recently, by Prencipe and Nestola (2007) who determined the variation of the critical bond radii between P = 1 atm and 28.4 GPa in beryl, through the analysis of Bader, for Al (0.13) and for O (0.21) $\{[r_C(0) - r_C(P)]/r_C(0) \times 100$, Bader 1994$\}$.

HP evolution of the $I2/c$ configuration and $I2/c$-$P2_1/c$ transition

The $I2/c$ structures determined at 4.4 and at 6.2 GPa show only minor modifications mainly involving shortening of the average <M-O> distances (Table 3). In particular, the O_A(2)-O_A(2) "strut" along **a*** ($\overline{AB}$ in Fig. 1b) decreases from 8.68 to 8.56 Å, due to the shortening of the M-O_A(2) distance (from 2.36 to 2.33 Å) and the M-M distance (from 3.97 to 3.91 Å). The O_A(2)-O_A(2) distance across the tetrahedral cage ($\overline{BC}$) remains constant at approximately 6.17 Å. The total variation of the O_A(2)-O_A(2) distances across the M-polyhedra and the tetrahedral cage ($\overline{AC}$ in Fig. 1b), corresponding to the variations as a function of pressure of the $2d_{100}$ distance, decreases from 14.85 to 14.73 Å. The $2d_{100}$ distance, which can be calculated from the unit-cell parameters reported by Nestola et al. (2004), shows a linear decrease in the pressure range 4.4–7.1 GPa where the $I2/c$ structure is stable (Fig. 7).

The $I2/c$-$P2_1/c$ transition at ~7.3 GPa involves a reduction of the symmetry with the loss of the twofold rotation axes and

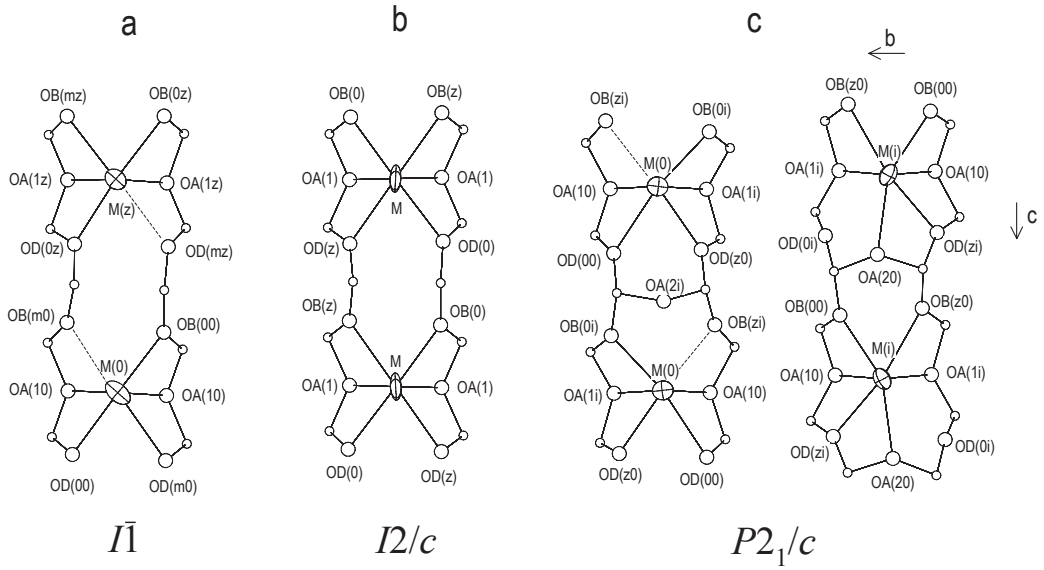

FIGURE 5. Partial coordinations of the non-tetrahedral Ca/Sr cations projected on the (100) plane. Tetrahedral T atoms are not labeled. (**a**) M(0)- and M(z)-polyhedra at P = 1 atm. (**b**) Single M-polyhedron at P = 4.4 GPa. (**c**) M(0)- and M(i)-polyhedra at P = 7.4 GPa. In $P2_1/c$ space group the two projections are at different heights: $x_{M(0)} = 0.539$ and $x_{M(i)} = 0.012$.

one-half of the centers of symmetry. In the P lattice the numbers of independent atomic sites is doubled and pairs of atoms related by the pseudo-body centering (**a** + **b** + **c**)/2 vector are present. Considering the two types of four-membered rings of the crankshaft chain running parallel to the **a** axis, one normal to **b** and the other approximately normal to **a** (Ribbe 1983), the symmetry centers retained in $P2_1/c$ space group lie in the centers of four-membered rings of tetrahedra approximately normal to the **a** axis, with ring-planes near ($\bar{1}$ 0 2). In Figure 8 the non-equivalent four-membered rings of tetrahedra around the symmetry centers are projected on the ($\bar{1}$ 0 2) plane in the $I2/c$ and $P2_1/c$ structures. The differences between the unique rings are increased in $P2_1/c$ in comparison with the $I2/c$ configuration, indicating the much more pronounced deformation of the tetrahedral framework. The modifications observed are related to the significant variations of the T-O-T angles, particularly to the changes of the average < T-O_C-T > angles that reduce to 117° in $P2_1/c$ configuration (Fig. 4). As observed by Angel et al. (2005), the T-O_C-T angle, which undergoes the greatest decrease with increasing pressure in feldspars, is the "hinge" of the crankshaft-chains closing up. In our work, the $T_2(00)$-$O_C(0i)$-$T_1(0i)$ angle (Fig. 8c) decreases to 104°, much lower than the 115° value, which is often considered an extreme limit for T-O-T angles in feldspars (Benusa et al. 2005). The very small value of this angle in $An_{20}SrF_{80}$ feldspar at P = 7.4 GPa is related to the large changes in the O_C oxygen atoms in the M(0)-polyhedron. In the compression of low albite, Benusa et al. (2005) observed that the biggest structural changes are the reduction in the T-$O_B(0)$-T and T-$O_C(0)$-T bond angles, with the $T_1(0)$-$O_C(0)$-$T_2(m)$ angle reaching the smallest value of 113.7° at P = 9.4 GPa. Moreover, in $An_{20}SrF_{80}$ feldspar, the $I2/c$-$P2_1/c$ transition also induces significant modifications of the internal O-T-O bond angles within the tetrahedra. The most deformed tetrahedron is the $T_2(00)$ (Fig. 8c), with the $O_A(20)$-$T_2(00)$-$O_C(0i)$ angle of 91° and the $O_C(0i)$-$T_2(00)$-$O_D(0i)$ angle

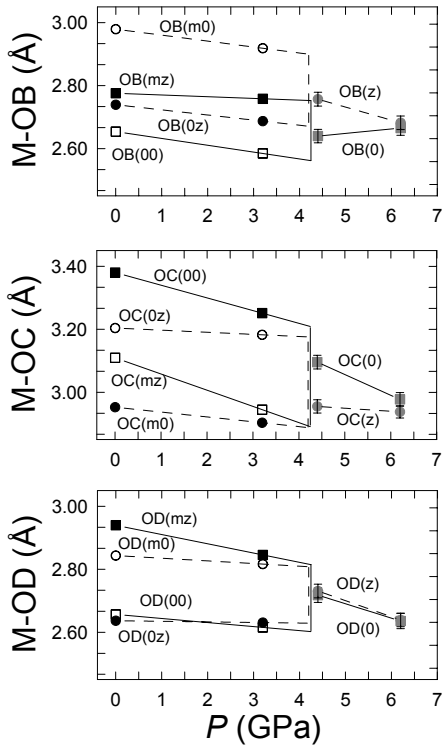

FIGURE 6. The variations of the M-O distances with pressure up to 6.2 GPa. The $I\bar{1}$-$I2/c$ transition is at ~4.3 GPa. The lines are drawn as guides to the eye. Triclinic $I\bar{1}$ configuration: squares = (00) and (mz) pseudo-related oxygen pairs; circles = (0z) and (m0); open symbols = M(0)-polyhedron; filled symbols = M(z)-polyhedron; symbol size exceeds the e.s.d. values. Monoclinic $I2/c$ configuration: gray squares = (0) oxygen, gray circles = (z) oxygen, bars indicate e.s.d. values.

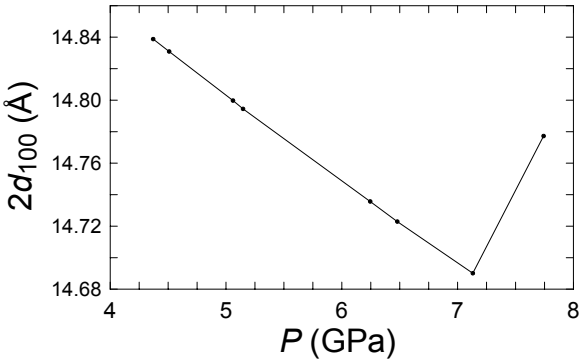

FIGURE 7. The variation with pressure of the $2d_{100}$ distance, calculated from the unit-cell parameters reported by Nestola et al. (2004) in the pressure interval 4.4–7.7 GPa.

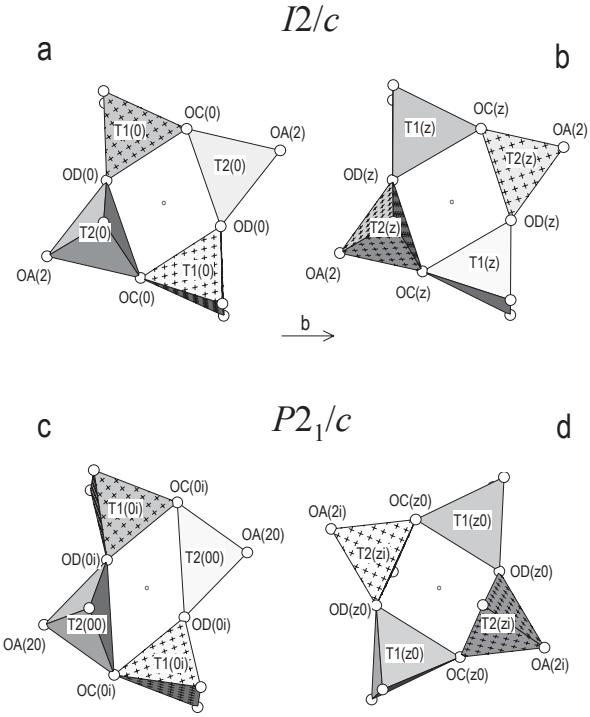

FIGURE 8. The four-membered rings of tetrahedra around the symmetry centers, approximately normal to the **a** axis, with ring-planes near $(\bar{1}\ 0\ 2)$. Projection on $(\bar{1}\ 0\ 2)$ plane; the $[\bar{2}\ 0\ \bar{1}]$ direction is vertical. Si-rich tetrahedra are hachured. $O_A(1)$ and O_B oxygen atoms are not labeled. (**a**) and (**b**) The two unique rings in $I2/c$ configuration at P = 4.4 GPa; centers at 1/4, 1/4, 1/4 and 1/4, 1/4, 3/4, respectively. (**c**) and (**d**) The most distorted (oblique) and the most regular (rectangular) of the four unique rings in $P2_1/c$ configuration at P = 7.4 GPa; centers at 0, 0, 0 and 1/2, 0, 1/2, respectively.

of 140° (Table 4). Small deviations from the true rigidity of the tetrahedra at high pressures were found in compounds with the quartz framework (Angel et al. 2005) and in the AlO_4 tetrahedra in microcline at 7 GPa (Allan and Angel 1997).

The other types of fourfold rings of tetrahedra characteristic for feldspars [those with (010) as the ring-plane] are represented

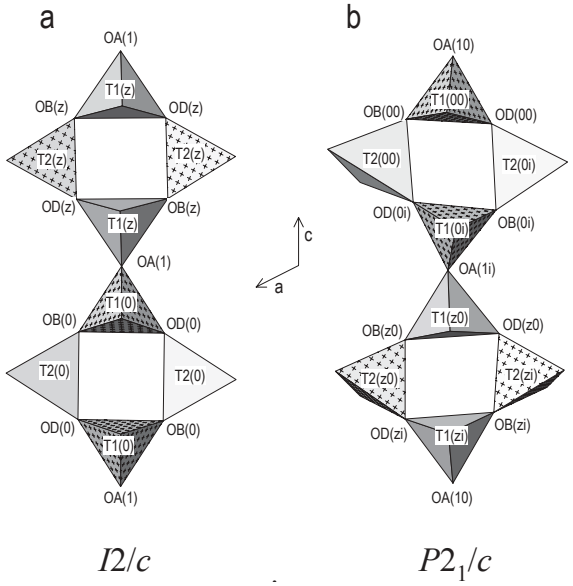

FIGURE 9. The four-membered rings of tetrahedra with (010) as the ring-plane, forming chains parallel to [001]. Projection on the (010) plane (thickness ~5 Å). Si-rich tetrahedra are hachured. $O_A(2)$ and O_C oxygen atoms are not labeled. (**a**) In $I2/c$ configuration, at P = 4.4 GPa, the rectangular rings are formed by the two pairs of equivalent tetrahedra; the twofold rotation axes, parallel to **b**, are at the centers of the rings. (**b**) In $P2_1/c$, at P = 7.4 GPa, the oblique rings consist of four symmetrically non-equivalent tetrahedra, as the twofold rotation axes are lost.

in Figure 9 at 4.4 and 7.4 GPa. Only in the $I2/c$ configuration are the rings formed by the two pairs of equivalent tetrahedra (Fig. 9a). Both in $I\bar{1}$ and in $P2_1/c$ they consist of four symmetrically non-equivalent tetrahedra (Fig. 9b). Whereas in $I\bar{1}$ and $I2/c$ the rings retain a shape almost ideally rectangular, in $P2_1/c$ their obliquity becomes evident (Fig. 9b). This again emphasizes a much more pronounced deformation of the tetrahedral framework in the very high-pressure $P2_1/c$ phase. A significant shear of the four-membered rings of tetrahedra was also observed by Benusa et al. (2005) in low albite at high pressure.

In conclusion, in $An_{20}SrF_{80}$ feldspar, the $I2/c$-$P2_1/c$ transition causes a significant distortion of the framework and a deformation of the tetrahedra, but does not involve a variation of the alternation of the Si- and Al-rich tetrahedra (Fig. 3).

The configurations of the M(0)- and M(i)-polyhedra [projected on the (100) plane in Fig. 5 and on the (001) plane in Fig. 10], resulting from the doubling of the single M-site of the $I2/c$ structure, are considerably different, with relevant changes in the coordination environment. In M(0)-polyhedron the larger variation concerns the $O_C(0i)$ and $O_C(zi)$ oxygen atoms that move closer to the cation and are therefore in the coordination sphere (Fig. 10b), whereas the $O_B(zi)$ oxygen (Fig. 5c) moves away. Considering all individual M(0)-O bond distances smaller than 2.91 Å (Table 3), there is not a clear gap to allow for a definition of the coordination number, which can therefore be assumed to be between 8 and 9. In the M(i)-polyhedron, the O_C atoms are at distances of ~3 Å as in all other feldspars (Fig. 10b), but in this case a second $O_A(20)$ oxygen comes into the first coordina-

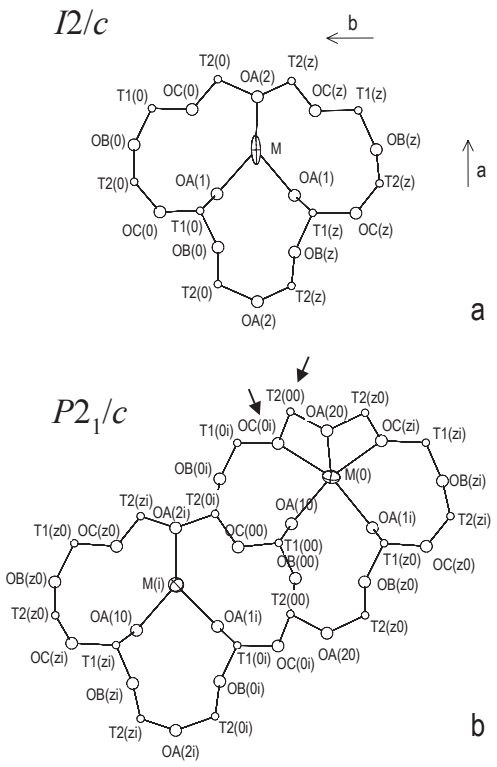

FIGURE 10. "Dog face" projections on the (001) plane (thickness ~2.7 Å). (**a**) The configuration around M-site in *I*2/*c* structure at $P = 4.4$ GPa. (**b**) The two different configurations around M(0)- and M(i)-sites at $P = 7.4$ GPa ($P2_1/c$ structure). In M(0) the two O_C oxygen atoms are coordinated; the arrows indicate the smallest T-O_C-T angle [$T_2(00)$-$O_C(0i)$-$T_1(0i)$ = 104°] and the most deformed $T_2(00)$ tetrahedron, with the $O_A(20)$-$T_2(00)$-$O_C(0i)$ angle of 91°.

tion sphere (Fig. 5c) and, at the same time, one of the bonds to O_D atoms is broken [M(i) – O_D(0i) = 3.05 Å]. Therefore, the coordination number for M(i) does not increase and remains 7. These changes are probably due to the stabilization of the very deformed and strained tetrahedral framework, which results from a change in the pattern of the M-O bonds.

The $2d_{100}$ distance, which decreases linearly between 4.4–7.1 GPa (Fig. 7), increases significantly at the transition to the $P2_1/c$ space group. This is due to the increase of the $O_A(2)$-$O_A(2)$ distances across the M-polyhedra along **a*** in the high-pressure $P2_1/c$ structure ($\overline{AB}$ in Fig. 1c), a change that is only partially compensated for by the shortening of the $O_A(2)$-$O_A(2)$ distance across the tetrahedral cage ($\overline{BC}$ in Fig. 1c). This suggests that, with increasing pressure, the M-M distance reaches the maximum compression compatible within the *I*2/*c* symmetry and, at higher pressures, the M-M repulsions do however play a role in the compression of the structure. In fact, the transition to $P2_1/c$ allows a relaxation of the M-M distance, which increases from 3.91 to 4.08 Å between 6.2 and 7.4 GPa.

In spite of the clear increase of the $2d_{100}$ distances at the transition to $P2_1/c$ (Fig. 7), the *a* cell parameter increases only slightly due to the decrease in the β angle from 114.94° to 114.17° between 7.1 and 7.7 GPa (Nestola et al. 2004). Moreover, the *I*2/*c*-$P2_1/c$ transition induces a large contraction of the *b* unit-cell parameter. This is probably due to the compression in the M(0)-polyhedron along **b**, which is essentially related to the dramatic decrease of the M(0)-O_C(0i) and M(0)-O_C(zi) distances (Fig. 10b) to unusually small values (2.54 and 2.57 Å, respectively).

ACKNOWLEDGMENTS

Reviews from R.J. Angel and an anonymous referee greatly improved the manuscript; we thank them for their critical reading and helpful suggestions. We are grateful to M. Prencipe for helpful discussions of the Bader theory, G. Ivaldi and G. Ferraris for critical review of some parts of the manuscript. We thank Eleda Johnson (Virginia Tech) for revising the English text. Financial support has been provided by MUR (Roma), CNR IGG (Torino), Danish Research Agency (Copenhagen), and Sofja Kovalevskaja Award (Bayreuth).

REFERENCES CITED

Allan, D.R. and Angel, R.J. (1997) A high-pressure structural study of microcline ($KAlSi_3O_8$) to 7 GPa. European Journal of Mineralogy, 9, 263–275.

Allan, D.R., Miletich, R., and Angel, R.J. (1996) Diamond-anvil cell for single-crystal X-ray diffraction studies to pressures in excess of 10 GPa. Review of Scientific Instruments, 67, 840–842.

Angel, R.J. (1988) High-pressure structure of anorthite. American Mineralogist, 73, 1114–1119.

——— (1994) Feldspars at high pressure. In I. Parsons, Ed., Feldspars and their reactions, p. 271–312. Kluwer, Dordrecht, The Netherlands.

Angel, R.J., Hazen, R.M., McCormick, T.C., Prewitt, C.T., and Smyth, J.R. (1988) Comparative compressibility of end-member feldspars. Physics and Chemistry of Minerals, 15, 313–318.

Angel, R.J., Ross, N.L., and Zhao, J. (2005) The compression of framework minerals: beyond rigid polyhedra. European Journal of Mineralogy, 17, 193–199.

Bader, R.F.W. (1994) Atoms in molecules, a quantum theory. International Series of Monographs on Chemistry, 22, Oxford University Press, U.K.

Baur, W.H., Joswig, W., and Müller, G. (1996) Mechanics of the feldspar framework; crystal structure of Li-Feldspar. Journal of Solid State Chemistry, 121, 12–23.

Benna, P. and Bruno, E. (2003) Single-crystal in situ high-temperature structural investigation of the $I\bar{1}$-*I*2/*c* phase transition in $Ca_{0.2}Sr_{0.8}Al_2Si_2O_8$ feldspar. American Mineralogist, 88, 1532–1541.

Benusa, M.D., Angel, R.J., and Ross, N.L. (2005) Compression of albite, $NaAlSi_3O_8$. American Mineralogist, 90, 1115–1120.

Bruker (2000) SMART, SAINT+ and XPREP. Bruker AXS Inc., Madison.

Bruno, E. and Facchinelli, A. (1974) Correlations between the unit-cell dimensions and the chemical and structural parameters in plagioclases and in alkaline-earth feldspars. Bulletin de la Société française de Minéralogie et de Cristallographie, 97, 378–385.

Bruno, E. and Gazzoni, G. (1968) Feldspati sintetici della serie $CaAl_2Si_2O_8$-$SrAl_2Si_2O_8$. Atti dell' Accademia delle Scienze di Torino, 102, 881–893.

Dove, M.T. and Redfern, S.A.T. (1997) Lattice simulation studies of the ferroelastic phase transitions in disordered (Na, K)$AlSi_3O_8$ and ordered (Sr, Ca)$Al_2Si_2O_8$ feldspar solid solutions. American Mineralogist, 82, 8–15.

Downs, R.T., Hazen, R.M., and Finger, L.W. (1994) The high-pressure crystal chemistry of low albite and the origin of the pressure dependency of Al-Si ordering. American Mineralogist, 79, 1042–1052.

Downs, R.T., Yang, H., Hazen, R.M., Finger, L.W., and Prewitt, C.T. (1999) Compressibility mechanisms of alkali feldspars: New data from reedmergnerite. American Mineralogist, 84, 333–340.

Hackwell, T.P. (1993) Feldspars at high pressures and temperatures. Ph.D. thesis, University of London, U.K.

Hackwell, T.P. and Angel, R.J. (1992) The comparative compressibility of reedmergnerite, danburite and their aluminium analogues. European Journal of Mineralogy, 4, 1221–1227.

Hazen, R.M. (1976) Sanidine: predicted and observed monoclinic-to-triclinic reversible transformations at high pressure. Science, 194, 105–107.

Kempster, C.J.E., Megaw, H.D., and Radoslovich, E.W. (1962) The structure of anorthite $CaAl_2Si_2O_8$. I. Structure analysis. Acta Crystallographica, 15, 1005–1017.

King, H.E. and Finger, L.W. (1979) Diffracted beam crystal centering and its application to high-pressure crystallography. Journal of Applied Crystallography, 12, 374–378.

McGuinn, M.D. and Redfern, S.A.T. (1994) Ferroelastic phase transition along the join $CaAl_2Si_2O_8$–$SrAl_2Si_2O_8$. American Mineralogist, 79, 24–30.

Megaw, H.D. (1970) Structural relationship between coesite and feldspars. Acta Crystallographica, B26, 261–265.

Nager, H.E. (1969) Strontiumfeldspat und die Mischreihe (Sr,Ca)[$Al_2Si_2O_8$]. Diplomarbeit, University of Münster.

Nager, H.E., Hoffmann, W., and Nissen, H.U. (1969) Die Mischreihe (Ca,Sr)[$Al_2Si_2O_8$]. Naturwissenschaften, 56, 136.

Nestola, F., Boffa Ballaran, T., Benna, P., Tribaudino, M., and Bruno, E. (2004) High-pressure phase transitions in $Ca_{0.2}Sr_{0.8}Al_2Si_2O_8$ feldspar. American Mineralogist, 89, 1474–1479.

Prencipe, M. and Nestola, F. (2007) Minerals at high pressure. Mechanics of compression from quantum mechanical calculation in a case study: the beryl ($Al_4Be_6Si_{12}O_{36}$). Physics and Chemistry of Minerals, 34, 37–52.

Prewitt, C.T. and Downs, R.T. (1998) High-pressure crystal chemistry. In R.J. Hemley, Ed., Ultrahigh-Pressure Mineralogy: Physics and Chemistry of the Earth's Deep Interior, 37, p. 282–317. Reviews in Mineralogy, Mineralogical Society of America, Chantilly, Virginia.

Ribbe, P.H. (1983) The chemistry, structure and nomenclature of feldspars. In P.H. Ribbe, Ed., Feldspar Mineralogy, 2, p. 1–20. Reviews in Mineralogy, Mineralogical Society of America, Chantilly, Virginia.

——— (1994) The crystal structures of the aluminum-silicate feldspars. In I. Parsons, Ed., Feldspars and their reactions, p. 1–49. Kluwer, Dordrecht, the Netherlands.

Ross, N.L. (2000) Framework structures. In R.M. Hazen and R.T. Downs, Eds., High-Temperature and High-Pressure Crystal Chemistry, 41, p. 257–287. Reviews in Mineralogy and Geochemistry, Mineralogical Society of America, Chantilly, Virginia.

Sheldrick, G.M. (1997) SHELXL-97—A program for crystal structure refinement, Release 97-2. University of Goettingen, Germany.

Tribaudino, M., Benna, P., and Bruno, E. (1993) $I\bar{1}$-$I2/c$ phase transition in alkaline-earth feldspars along the $CaAl_2Si_2O_8$–$SrAl_2Si_2O_8$ join: Thermodynamic behaviour. Physics and Chemistry of Minerals, 20, 221–227.

MANUSCRIPT RECEIVED JULY 31, 2006
MANUSCRIPT ACCEPTED MARCH 15, 2007
MANUSCRIPT HANDLED BY MARTIN KUNZ